Applied Surface Science 594 (2022) 153427

Contents lists available at ScienceDirect

Applied Surface Science

journal homepage: www.elsevier.com/locate/apsusc

Full Length Article

Control of ultrafast laser ablation efficiency by stress confinement due to strong electron localization in high-entropy alloys

David Redka [a,b,*], Jan Winter [a,c], Christian Gadelmeier [d], Alexander Djuranovic [a], Uwe Glatzel [d], Ján Minár [b], Heinz Paul Huber [a,**]

[a] Munich University of Applied Sciences HM, Department of Applied Sciences and Mechatronics, Lothstr. 34, 80335 Munich, Germany
[b] New Technologies-Research Center, University of West Bohemia, Univerzitní 8, 30100 Plzeň, Czech Republic
[c] Erlangen Graduate School in Advanced Optical Technologies (SAOT), Friedrich-Alexander-Universität Erlangen-Nürnberg, Paul-Gordon Straße 6, 91052 Erlangen, Germany
[d] Metals and Alloys, University of Bayreuth, Prof.-Rüdiger-Bormann-Str. 1, 95447 Bayreuth, Germany

ARTICLE INFO

Keywords:
High-entropy alloy
CrMnFeCoNi
Ultrafast laser ablation
Pulse duration
Ablation efficiency
Stress confinement

ABSTRACT

In the context of current state of the art, understanding the laser ablation efficiency decrease for pulse durations exceeding the mechanical relaxation time of a few ps remains a pending research question. A heuristic approach may be used to reveal the role of effective penetration depth on ablation efficiency. Extending familiar contributions of this quantity by a term related to the mechanical surface expansion during pulse irradiation, the relation of ablation efficiency and pulse duration is deciphered. Thus, longer pulses are coupled into an expanded surface, revealing a direct link to the violation of stress confinement. To best demonstrate this hypothesis, a material with high electron–phonon coupling as well as low thermal conductivity, i.e., strong electron localization, is required. These properties are accomplished by high-entropy alloys, and the CrMnFeCoNi alloy serves as prime candidate. We report on single-pulse ablation efficiency experiments of the CrMnFeCoNi alloy which are support by our proposed model.

1. Introduction

Laser micro-machining of metals using ultrashort pulse (USP) lasers has gained exceptional industrial relevance as well as scientific attention. Besides theoretical explanations [1–4], quality optimization and efficiency increase [5–10] remains a central topic of investigation. In general, micro-machining using USP laser, typically in the sub to few ps range, beats corresponding nanosecond systems, mainly in terms of surface quality and precision [11,12]. Well-defined crater edges as well as a reduced heat-affected zone, yields less material modification around the ablation crater [13–15], making USP laser an indispensable tool in modern fabrication processes [16]. The crucial throughput optimization may be achieved by increasing laser repetition rates as well as scanning speeds. However, the ablation efficiency, and subsequently the throughput, was also shown to be governed by the pulse duration, with a higher ablated volume per pulse energy for sub-ps in comparison to ps pulses [6,17]. For example, machining of stainless steel with 30 ps pulses results in a 80 % decreased ablation efficiency of 1.1 $\mu m^3/\mu J$ compared to 5.7 $\mu m^3/\mu J$ at 3 ps [6]. This decrease during the transition from sub ps to picosecond pulse durations is quasi-independent of the investigated metal and located at 3 – 5 ps [17].

The absorption of USP laser radiation by conduction band electrons of a metal is sufficiently described by the Beer-Lambert model with an corresponding optical penetration depth δ_{opt} [18]. For pulse durations below the internal thermalization time of electrons (some tens to 100 fs [19,20]), a non-fermi-like distribution of the electrons will be induced [21]. In contrast, exceeding some hundreds of fs in pulse duration, a direct heating of conduction electrons is proposed [17], yielding a local increase of the electron temperature [22]. Subsequent energy dissipation from the hot electrons takes place via thermal diffusion with the diffusion coefficient given by $D_{th} = \langle \delta_{diff}^2 \rangle / 2t$, with δ_{diff} and t the diffusion length and time, respectively. In parallel to the electronic thermal conduction [23], heat is transferred to the cold lattice by electron–phonon scattering (electron–phonon coupling [22]), where thermal equilibrium for both subsystems is typically established after τ_{ep} with

* Corresponding authors.
** Corresponding authors.
E-mail addresses: dredka@hm.edu (D. Redka), heinz.huber@hm.edu (H.P. Huber).

https://doi.org/10.1016/j.apsusc.2022.153427
Received 12 January 2022; Received in revised form 24 February 2022; Accepted 15 April 2022
Available online 26 April 2022

few picoseconds [17,24]. As a result, the lattice heating time is limited by τ_{ep} or the pulse duration τ_p, whichever is longer. If the lattice heating time is shorter than the mechanical relaxation time $\tau_{mech} = \delta_{opt}/c_s$ [25], where c_s is the speed of sound, the process is quasi-isochoric. In conclusion the pressure build-up within the energy absorption depth is maximized [25]. This situation is called fulfillment of stress confinement, written as $\max\{\tau_{ep}, \tau_p\} \leq \tau_{mech}$ [26,27], where for transition metals τ_{mech} is in the range of 3 ps to 5 ps [17]. The resulting pressure amplitude with values up to tens of GPa [1,2,25] propagates into the material as well towards the surface, where it is partially reflected and due to the impedance mismatch transformed to a rarefaction wave [25,28]. This rarefaction causes the material surface to expand already after some ps, known as early mechanical motion δ_{disp} [29,30]. Experimental observations using pump–probe interferometry [30] or pump–probe ellipsometry [2,29] reveal velocities of around 1 km/s [30] and a density decrease of 30 – 40 % [29]. Exceeding the spall-strength of the already liquefied metal, material fracture may be induced [27]. This spallation or photomechanical ablation [1] describes the delamination of a thin layer (some few tens of nm) usually for a few multiple of the ablation threshold fluence Φ_{thr} [17]. Phase explosion or photothermal ablation is found for higher fluences or increasing pulse durations, where the maximum surface temperature of the lattice rises and vaporization or supercritical boiling (0.9 T_c, with T_c the critical temperature [31]) takes place. A simple heuristic description relates the ablation depth to the applied laser peak fluence Φ_0 with $\delta_{abl} = \delta_{eff} \ln(\Phi_0/\Phi_{thr})$ [32], where ablation occurs when the local energy density exceeds Φ_{thr}. The effective penetration depth is given by $\delta_{eff} = \delta_{opt} + \delta_{diff}$ [33] (δ_{diff} diffusion length at $t = \tau_p$), whereas the surface displacement is still not considered. Therefore, Winter et al. [17] introduced a subtractive term in order to describe the remarkable decrease of the effective penetration depth for longer pulse durations. Therefore we are able to quantify the observed decrease of ablation efficiency in a heuristic model, since according to Furmanski *et al.* the ablation efficiency is proportional to δ_{eff}/Φ_{thr} [32].

Minimizing the contribution of thermal conductivity on δ_{eff} is therefore a key step towards understanding the ablation efficiency regarding the pulse duration. A low electron–phonon coupling time in turn permits the lattice heating time to be controlled directly by the pulse duration, mirroring the transient surface displacement. Therefore the CrMnFeCoNi high-entropy alloy (HEA), also referred as Cantor alloy [34] serves as an excellent material of investigation. The strong electron localization in terms of a retarded electron mobility, attributed to the reduced mean free path length of the electrons [35,36], leads to a minimized thermal diffusivity of the electrons (3.5 nm^2/ps [37] at standard conditions) as well as to a maximized electron–phonon coupling. Mass fluctuations of elements in HEAs lead to phonon broadening, which significantly depresses the contribution of phonon thermal conductivity [38]. On the other hand, thermodynamic properties (phase transition enthalpies or temperatures) are not substantial affected by the retarded electron mobility [37,39]. Since thermodynamic and transport properties are crucial parameters for understanding ultrafast laser ablation, HEAs provide an ideal illustration for the stress confinement hypothesis and are therefore best suited for the isolation of the effect of early mechanical motion on the ablation efficiency. The aim of this work is to test the stress confinement hypothesis with an extension of a well-established heuristic model by quantifying the correlation between δ_{disp} and the ablation efficiency of metals. Consequently single pulse experiments (avoid accumulation effects [9]) with pulse durations of 0.5 ps $< \tau_{mech} <$ 20 ps are meticulously performed and the final state observables as ablation energetics or crater morphology are evaluated with regard to a heuristic model approach.

2. Materials and Methods

2.1. CrMnFeCoNi manufacturing and sample preparation

The polycrystalline CrMnFeCoNi alloy sample was manufactured in-house from pure elements (at least 99.99 %). Master alloys were prepared which were then cast into a cylindrical shape with a diameter of 20 mm and a length of 110 mm and directly solidified in [001] direction using the Bridgeman method [40]. The maximum deviation from the uniform distribution along the rod was less than 1 at. % for all five elements and the grain size was 150 µm to 180 µm. For the ablation experiments, 1 mm thick discs were cut off, embedded in epoxy resin and planar ground with a 400 SiC paper. Subsequent polishing with (9, 3 and 1) µm polycrystalline diamond suspensions resulted in a root mean square surface roughness of 1.2 nm. A detailed description of the manufacturing process, sample preparation and analysis of the sample quality can be found in our previous works [39,40].

2.2. Experimental setup

All single-pulse experiments were performed with a femtosecond laser source (*Spectra Physics* FemtoREGEN) emitting pulses with a constant repetition rate of 500 Hz and a pulse energy E_p of 60 µJ (pulse-to-pulse fluctuations below 1 %). The central wavelength is 1056 nm with a spectral width of 5 nm (FWHM), and the pulse duration (FWHM, $sech^2$ temporal profile) is 600 fs. The fluence ($\Phi_0 = 2E_p/(\pi w_0^2)$) of the individual pulses during material processing was adjusted by a lambda-half wave plate - beam splitter combination and the Gaussian beam (beam quality $M^2 < 1.4$) was focused on the CrMnFeCoNi alloy substrate by a plano-convex lens with a focal length of $f = 100$ mm. The resulting beam waist radius was 13.5(4)µm (e^{-2} intensity), calculated by the D^2 method, and double checked with a beam caustic measurement with 14.8(8)µm (*PRIMES* MicroSpotMonitor), which was in good agreement. For the pulse duration dependent measurements, a pulse stretcher setup was used [41,42], allowing pulse durations from 0.5 ps up to 20 ps to be set. In the ablation experiments, for each fluence and pulse duration applied, the experiments were repeated five times and all results were averaged. In this work, the pulse duration τ_p was varied from 0.5 ps to 20 ps and the peak fluence Φ_0 from 0.1 J/cm^2 to 10 J/cm^2, where the remaining laser parameters were kept constant. All fluences in this work are irradiated fluences.

2.3. Ablation threshold and crater morphology determination

For all ablation craters, the ablation diameter D was measured using light microscopy imaging (*Leitz* Ergoplan (50x/0.85)). The quantitative determination of the ablation threshold Φ_{thr} and the beam waist radius w_0 (e^{-2} intensity) was carried out according the D^2 method [43]

$$D^2 = 2w_0^2 \ln(\Phi_0/\Phi_{thr}). \quad (1)$$

The crater surface topography was measured using an optical surface profiler (*Sensofar* Plµ 2300 (50x/0.42), interferometric mode) with a lateral and axial resolution of 570 nm and 0.1 nm, respectively. The crater profiles, depths and volumes were acquired from these data using the Gwyddion software (Ver. 2.56, released 30 June 2020). Scanning electron microscope (SEM) measurements (*TESCAN* LYRA3) were performed to show the ablation crater morphology. The energy specific ablation volume (*ESAV*) or ablation efficiency in brief was calculated by dividing the measured ablation volumes by the corresponding irradiated pulse energies.

3. Results

3.1. Pulse duration dependent ablation thresholds

Single pulse laser ablation experiments were performed on a CrMnFeCoNi alloy substrate with fluences up to 10 J/cm^2, pulse durations between 0.5 ps and 20 ps and a laser wavelength of 1056 nm. Fig. 1a (red circles, right axis) shows the pulse duration dependence of the ablation threshold. The fluence and pulse duration resolved crater diameters (D^2 measurements), used to determine the depicted values, are given in sFigure 2 of the supplementary materials. At 0.5 ps pulse duration, the evaluated ablation threshold Φ_{thr} is 0.24(1) J/cm^2, which is consistent with our previous work [39]. Assuming that a specific energy density threshold leads to material ablation, for example, by reaching the evaporation enthalpy, which is $\Delta H_v = 47.4$ J/mm^3 for the CrMnFeCoNi alloy, the ablation threshold can be estimated via $\Phi_{thr} \approx \delta_{opt}\Delta H_v/(1-R)$ [11,44]. For the CrMnFeCoNi alloy the reflectance is given with $R = 0.707(1)$ [39] and the optical penetration depth by $\delta_{opt} = 15.6(1)$ nm [39] at our laser wavelength of 1056 nm. This gives an estimate of 0.25(1) J/cm^2, which agrees well with our experimental value. The correspondence of absorbed laser energy density and evaporation enthalpy experimentally proves that the assumption of evaporation is energetically in a first order approximation a sufficient ablation criterion. Further, as it is seen from Fig. 1a, the pulse duration dependent Φ_{thr} remains quasi-constant for τ_p up to about 5 ps and then increases steadily until a value of 0.31 J/cm^2 at 20 ps is reached. This corresponds to a rise of roughly 30 % within our investigated pulse durations. A rising threshold, as observed, is expected for longer pulse durations as energy dissipation into the material via heat diffusion already takes place during the pulse irradiation. The heat diffusion length during pulse irradiation τ_p is given for the case of established electron–phonon equilibrium by $\delta_{diff} = \sqrt{2D_{th}\tau_p}$ [33], with D_{th} the thermal diffusivity. By extending the optical penetration depth with the pulse duration-dependent diffusion length in the above-mentioned estimation of the threshold fluence, we obtain a $\sqrt{\tau_p}$ dependence for $\Phi_{thr}(\tau_p)$. In our measurements only the onset towards this relation is identified, where a clear square root dependence is usually observed for pulse durations above several 10 ps to 100 ps [45].

3.2. Crater profiles and effective penetration depth

Fig. 1b shows the crater cross sections for selected pulse durations at a laser peak fluence of 0.9(1) J/cm^2. As seen, for increasing pulse duration the crater depth in the ablation center decreases significantly, although the irradiated energy density remains constant. Furthermore, beginning from 10 ps, the previously pronounced parabolic crater profile changes in shape towards a rather rectangular cross-section. This effect is best seen in the comparison of the 0.5 ps (28(1) nm deep and parabolic) and 20 ps (12(1) nm deep and rectangular) ablation craters.

For materials with a specific threshold fluence and an exponentially

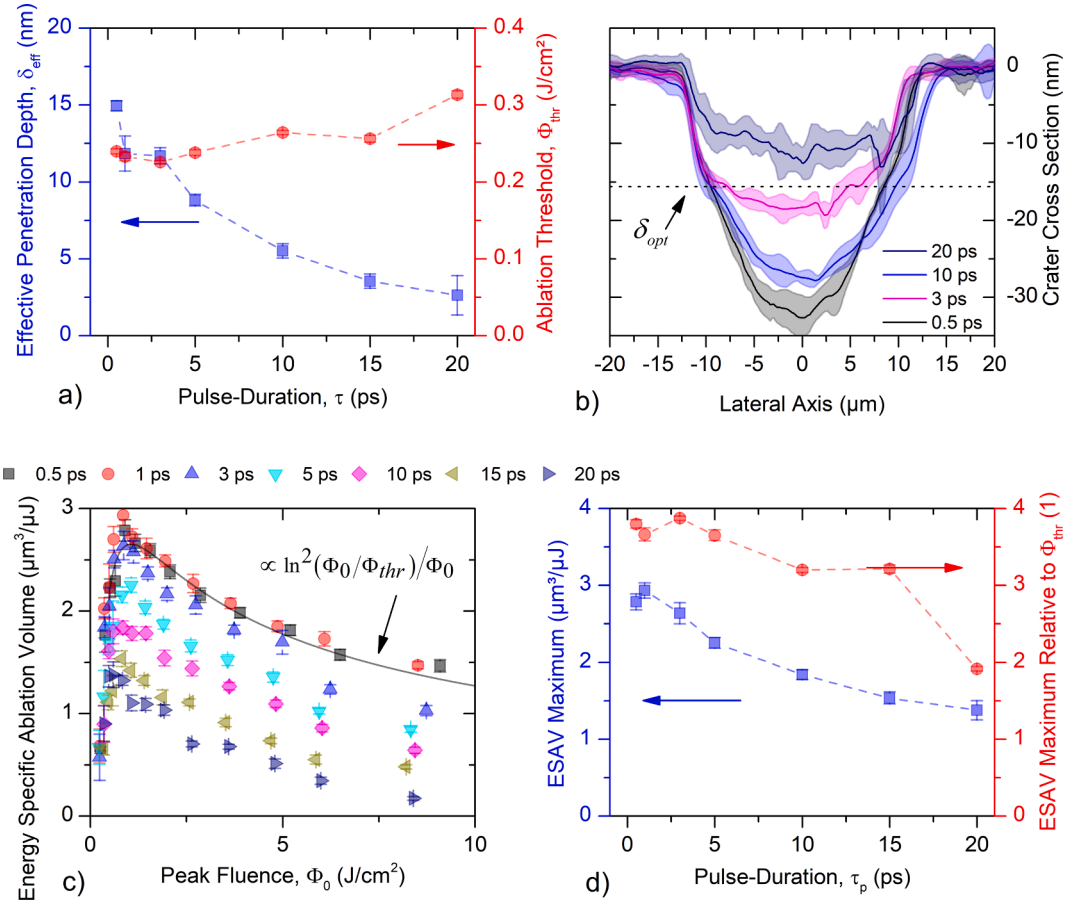

Fig. 1. Ablation thresholds, effective penetration depths, crater profiles and efficiency for the laser ablation of CrMnFeCoNi alloy at the investigated pulse durations. a) Pulse duration dependence of the ablation threshold (Red circles with dashed lines, right axis) and the effective penetration depth (blue squares with dashed line, left axis). b) Crater cross-sections at 0.9(1) J/cm^2 and low intensity optical penetration depth marked with δ_{opt}. c) Energy specific ablation volume, showing that the maxima decrease with increasing pulse duration. As a guide to the eye, equation (3) was fitted to the 0.5 ps pulse duration data. At the highest pulse duration, the maximum relative to the threshold shifts towards lower fluence values to such an extent that the fit can no longer be performed. d) Quasi-exponential decrease of the *ESAV* maximum (magenta diamonds) with pulse duration and shift of the maximum with respect to the ablation threshold (red squares).

decreasing energy density in the axial direction at the time of ablation, a phenomenological relationship between the ablation depth as well as the local applied fluence is given by [32]

$$d(\Phi_0) = \delta_{\mathrm{eff}} \ln(\Phi_0/\Phi_{\mathrm{thr}}). \quad (2)$$

Here δ_{eff} describes the effective penetration depth (e^{-1} energy density decrease), which is usually composed of the optical penetration depth and thermal diffusion [33]. Substituting an ideal Gaussian profile into equation (2) yields in the familiar parabolic crater profile [32]. However, this approximation fails in predicting the cross sections at higher pulse durations, since the rectangular crater cross-section indicates a homogeneous heated layer, as is the case for thin film ablation or a flat-top shaped beam profile.

The maximum ablation depths versus peak fluence are determined from the central region ($r < 1\,\mu\mathrm{m}$ and $\Phi(r)/\Phi_0 > 0.99$) of the measured crater surface topography (see sFigure 2b) and the effective penetration depth is evaluated using equation (2). The pulse duration dependent results are shown in Fig. 1a (blue squares, left axis). All fluence and pulse duration resolved crater profiles as well as the obtained ablation depths are available in the supplementary materials (see sFigure 3). The regression of Eqn. (2) to the measurement data was performed for all pulse durations only up to peak fluences of 3 J/cm^2, since for higher values deviations from the logarithmic behavior occur. For the shortest pulse duration of 0.5 ps we receive a value for the effective penetration depth of 14.9(3) nm which is in good agreement with the optical penetration depth of 15.6(1) nm [39], and corresponds to the expectation that the influence of thermal conduction is negligible for the short pulse duration. With increasing pulse duration, a quasi-exponential decrease of the effective penetration depth is found, where the value at 20 ps has reached 2.6(1.3) nm, corresponding to a reduction of about 80% in comparison to the 0.5 ps value. More remarkably, the effective penetration depth falls well below the value of the optical penetration depth, which inevitably indicates a counteracting effect during energy absorption.

Furthermore, it should be noted that the ablation thresholds determined by the δ_{eff} method with 0.14(1) J/cm^2 at 0.5 ps contradictory decrease towards longer pulse durations (see supplementary materials sFigure 4) and underestimate the values determined by the D^2 method [46]. This disagreement between both models is attributed to the formation of a minimum ablation depth, which corresponds to a spallation layer, and thus an extrapolation to the zero level misinterprets the actual ablation threshold [17].

3.3. Energy specific ablation volume

The **E**nergy **S**pecific **A**blation **V**olume (*ESAV*) or ablation efficiency in brief, which is defined as the ablated volume divided by the irradiated pulse-energy, is shown in Fig. 1c for the investigated pulse durations. Basically, for all pulse durations, the trend of the *ESAV* curve is comparable, so that the ablation efficiency increases up to a maximum value with a subsequent decrease. For 0.5 ps we determine an *ESAV* maximum of 2.8(1) μm^3/μJ which is located at 3.8 Φ_{thr}. This value remains roughly constant for pulse durations up to 3 ps and then decreases rapidly, until at 20 ps pulse duration the *ESAV* maximum is 1.4(1) μm^3/μJ. This decrease corresponds to a loss of 50 % in the ablation efficiency when compared to the values below 3 ps. The *ESAV* maxima extracted from the measured data (blue squares, left axis) and their location relative to the ablation threshold (red circles, right axis) are given in Fig. 1d. For pulse durations exceeding 3 ps, a significant decay of the *ESAV* maximum is clearly visible. In contrast, the location of the *ESAV* maxima relative to the ablation threshold remains approximately constant at a value of

$$ESAV = \frac{\delta_{\mathrm{eff}}}{2\Phi_0} \ln^2\left(\frac{\Phi_0}{\Phi_{\mathrm{thr}}}\right), \quad (3)$$

with its maximum located at e^2 Φ_{thr}. This model is in good agreement with experimental multi-pulse data [47], but for single-pulse experiments, as it is the case here, a lower Φ_{thr} is found, compared to the D^2 method [17,46]. This is again attributed to the formation of a spallation layer, as is the case in the determination of the effective penetration depth δ_{eff} (see Fig. 1a).

4. Discussion

In the results, the pulse duration dependent ablation thresholds, effective penetration depths and the *ESAV* measurements were shown and already briefly discussed. At this point we will discourse how this quantities take effect on the pulse duration dependent ablation efficiency. A straightforward heuristic mathematical description for the *ESAV* is given by equation (3), with a maximum located at e^2-times the ablation threshold. From our data, we found the deviation from e^2-times the threshold to be $\Phi_{\mathrm{max}} = 3.8\Phi_{\mathrm{thr}}$ at 0.5 ps, showing an increasing bias towards 1.9 Φ_{thr} at 20 ps pulse duration (see Fig. 1c), which is associated with the change in the ablation cross section characteristics (from parabolic to thin film). If this mismatch is considered in the calculation of the *ESAV* maximum, we obtain an appropriate equation for the determination of the pulse duration dependent ablation efficiency maximum

$$\max(ESAV) = 2\frac{\delta_{\mathrm{eff}}}{\Phi_{\mathrm{max}}}. \quad (4)$$

The *ESAV* maxima calculated from measured Φ_{max} and δ_{eff} according to Eqn. (4) are shown in Fig. 2a and compared with the ablation efficiencies determined from the volume measurements. It becomes apparent that our approximation is in good agreement with the measured ablation efficiency. At first glance, both curves clearly indicate the same constant behavior up to a pulse duration of about 3 ps, with a subsequent decay. However, this fall-off is somewhat more pronounced for the calculated data points (red circles in Fig. 2a). The constant ablation efficiency up to 3 ps is associated with the fulfilled stress confinement condition below $\tau_{\mathrm{mech}} = \delta_{\mathrm{opt}}/c_s$ [48], where c_s is the speed of sound in the liquid metal. For the CrMnFeCoNi alloy c_s of the liquid metal at the melting temperature is calculated by the rule of Gitis and Mikhailov [49] with $c_s \approx \sqrt{2\Delta H_v/M} \approx 3.4$ km/s, where $\Delta H_v = 332.4$ kJ/mol [39]and $M = 56.2$ g/mol are the molar enthalpy of vaporization and the equivalent molar mass of the alloy, respectively. The minimum mechanical relaxation time is calculated as $\tau_{\mathrm{mech}} \approx 4.5$ ps, which is in good agreement with the onset of the *ESAV* decrease at 3 ps. Thus for pulse durations below the minimum mechanical relaxation time, stress confinement is fulfilled and the ablation is strongly dominated by a high pressure build-up resulting in a rarefaction wave and thus causing a spall fracture of an already liquefied metal layer. This photomechanical ablation process (spallation) is also more energetically efficient (higher *ESAV* value) in contrast to a pure photothermal process like phase explosion or evaporation [1]. A transition between these ablation regimes is expected for pulse durations exceeding the minimum mechanical relaxation time, accompanied by a decrease in ablation efficiency. For pulse durations exceeding τ_{mech} the decay of the ablation efficiency corresponds also reasonably well with the effective penetration depth δ_{eff} (see Fig. 1a and 1d, blue squares). Further, we need to emphasize the influence of the effective penetration depth on the drop of the ablation efficiency maximum using the heuristic model according to equation (3). From the comparison of the effective penetration depths at 20 ps and 0.5 ps we find a relative decrease of δ_{opt} from 14.9(1) nm to 2.6(1.3) nm by 80 %. In contrast, the corresponding measured *ESAV* maximum values are at 50 %, namely from 2.8 μm^3/μJ to 1.4 μm^3/μJ. Thus, solely considering the effective penetration depth overestimates the *ESAV* decrease. However, taking into account the reciprocal proportionality of Φ_{max} raises the estimated *ESAV* values according to the measurement (see Fig. 1d), where the Φ_{max} value decreases from 3.8 J/cm^2 to 1.9 J/cm^3 by 50 %. The *ESAV* estimate from equation (4)

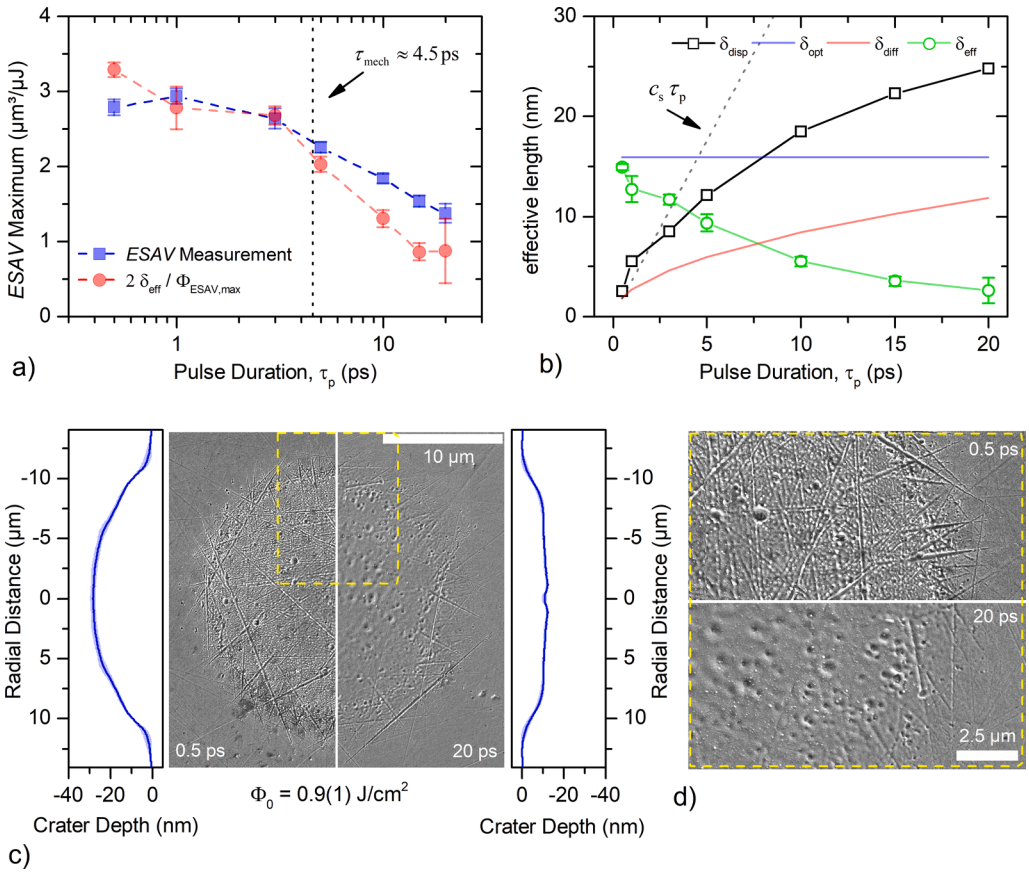

Fig. 2. Comparison of ablation efficiency, contributions to effective penetration depth and SEM images of the ablation craters. a) Comparison of the *ESAV* measurement (blue rectangles) the approximation according to equation (4) (red circles). b) Contributions to the effective penetration depth according to our model (equation Eqn 5) at time $\tau_p/2$. The contribution of the mechanical surface expansion increases more strongly with increasing pulse duration than the thermal diffusion length, which leads to a decrease in the effective penetration depth. c) SEM images of the ablation craters at a peak fluence of 0.9(1) J/cm^2 for the pulse duration of 0.5 ps and 20 ps. The corresponding crater cross sections are shown on the left / right. d) Magnification from the yellow dashed area from subfigure 3c.

corresponds to a drop of 60 %, which is in good agreement with the measurement of 50 %. It is also evident from the measurements that Φ_{max}, although only falling significantly from 10 ps (compare also the ablation crater characteristics from parabolic to rectangular in Fig. 1b), nevertheless continuously contributes to a hypothetical ESAV increase. From this it can be seen that the single parameter that leads to a decrease in the *ESAV* maximum is the effective penetration depth, which highlights the inherent significance in understanding the behavior of δ_{eff} as a function of pulse duration.

In order to model the pulse duration dependence of the effective penetration depth in a heuristic approach, we introduce the subtractive term for the surface displacement during pulse-irradiation, proposed by Winter et al. [17] as

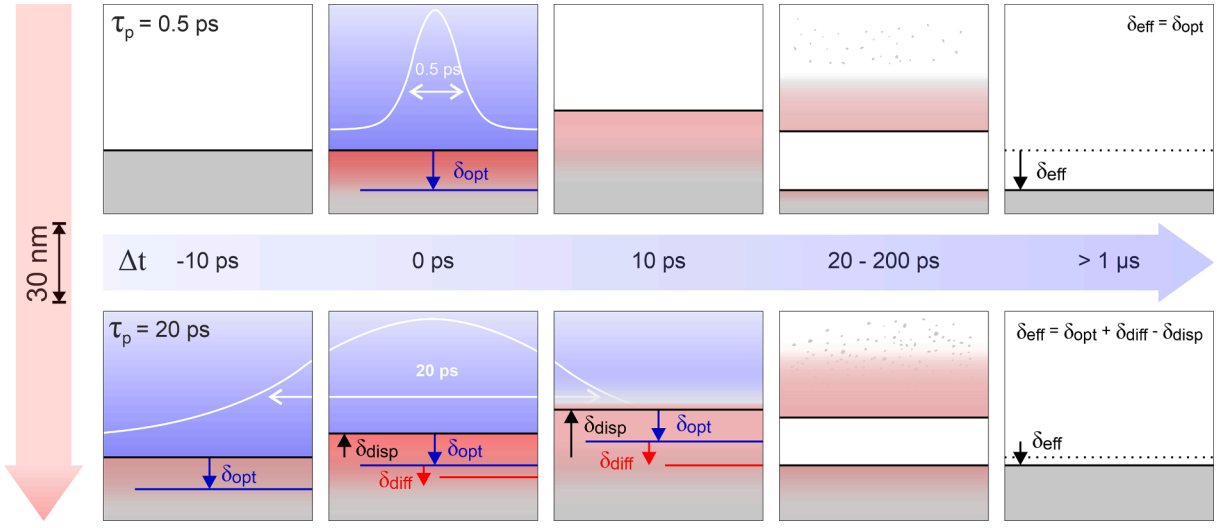

Fig. 3. Schematic sketch of the influence of the early mechanical motion on the effective penetration depth. One dimensional representation (center of Gaussian beam) of the heuristic model and the evolution of the single contributions within time. The upper row is representing the laser matter interaction of a 0.5 ps and lower row for a 20 ps single pulse. The 0.5 ps pulse has an effective penetration depth close to the optical penetration depth and for the 20 ps pulse the effective penetration (see 10 ps $= \tau_p/2$) depth is strongly reduced by the surface displacement during pulse irradiation, although heat diffusion takes place. The spallation, or film delamination is for both pulse durations depicted at 20 – 200 ps after pulse impact (fourth column) and the final ablation state is reached at a time of a few µs.

$$\delta_{\mathrm{eff}} = \delta_{\mathrm{opt}} + \delta_{\mathrm{diff}} - \delta_{\mathrm{disp}}. \quad (5)$$

By this, three relevant processes are considered, taking influence on the pulse duration dependence of the effective penetration depth. A schematic sketch of the model approach is shown in Fig. 3. Starting with the energy coupling of the laser irradiation within the optical penetration depth δ_{opt} of the metal, a local increase in the electron temperature is induced. This energy density distribution is subsequently, and for pulse durations of some ps already during the energy deposition, blurred out due to energy dissipation via heat diffusion of hot electrons into the material. The thermal diffusion if given by δ_{diff}. For metals with a low electron–phonon equilibrium time, only equilibrium heat conduction is taken into account, which is typically one to two orders of magnitude below the thermal conductivity of non-equilibrium thermal conductivity [33]. Typical magnitudes of τ_{ep} for pure transition metals with low electron–phonon interaction range from 10 ps for gold [50] to a few ps for aluminum (recalculated from [51]) as well as the pure constituents of the CrMnFeCoNi alloy [52]. Disordered systems further exhibit stronger electron–phonon coupling, as is the case for stainless steel with slightly above 1 ps [17,53,54]. Due to the extensive electron localization in the CrMnFeCoNi high entropy alloy [35], increased coupling is predicted, ensuring the assumption of pure equilibrium thermal conduction. With the third process, the early surface expansion, we obtain an opposite mechanism, which effectively reduces absorption length and heat diffusion length into the material. This approach allows us to explain the decrease of the effective penetration depth with pulse duration, since diffusion length and surface displacement during pulse irradiation show dependence on the pulse duration (see Fig. 3 comparison of δ_{eff} and the contributions for a 0.5 ps and 20 ps pulse).

In this regard, we have so far considered the optical penetration depth to remain constant. As this is a crucial assumption for our further considerations, we discuss, if the supposition of a constant optical penetration depth is justified under our experimental environment. From the dielectric function, using the Drude Model for the CrMnFeCoNi high-entropy alloy, the density dependence of the optical penetration depth (see supplementary materials Section 1) is given in an approximated form by $\partial\delta_{\mathrm{opt}}/\delta_{\mathrm{opt}} \approx -0.5\partial\rho/\rho$. Here ρ is the density of the metal. Winter et al. [29] showed from the analysis of the transient extinction coefficient, obtained by pump probe ellipsometry, that for aluminum a density decrease of around 50 % within the optical penetration depth after laser irradiation with a 0.7 ps pulse at 2.5 Φ_{thr} is found [29]. A comparable behavior for the CrMnFeCoNi alloy would, according to the given estimation, result in a dynamic increase of the optical penetration depth by 40 % (22 nm), especially for longer pulse durations. In parallel, the increase in electron temperature during pulse irradiation and eventually the effect on the dielectric function must be addressed. Two temperature model simulations of stainless steel show maximum electron temperatures at the surface of 40 kK when irradiated with ultrashort laser pulses of 100 fs and a fluence of 4 times the ablation threshold [55], accompanied by an increase of the optical penetration depth of maximum 40 % [55,56]. However, the maximum electron temperature for metals scales with $1/\tau_{\mathrm{p}}$ [18], since energy transfer from the electronic to the lattice subsystem already takes place during pulse irradiation. Therefore, the given variation represents an upper limit, which, however, is significant lower for longer pulse durations, especially above τ_{mech}. For the CrMnFeCoNi alloy, an equivalent relationship is expected due to the similarity of thermodynamic as well as electronic and optical properties [37,39,57,58]. Based on the given estimates, it follows that the optical penetration depth can increase during pulse irradiation to a maximum op up to 100 %. It follows, that for short pulse durations ($\tau_{\mathrm{p}} < \tau_{\mathrm{ep}} \approx 1$ ps, electron–phonon equilibrium time), the change in optical penetration depth is dominated by the maximized electron temperature, whereas for long pulse durations ($\tau_{\mathrm{p}} > \tau_{\mathrm{mech}}$), the density decrease during pulse irradiation plays a dominant role. Since both effects influence δ_{opt} in the same way and only partially overlap, on average the optical penetration depth will experience the maximum influence of a single contribution for all pulse durations. Thus, δ_{opt} would in practice exceed the steady state value up to factor 1.4, leading to a change from 15.6(1) nm to maximum 22 nm. In the following discussion we refrain from taking this value into account, since the influence is small and expected to be constant. The calculated surface displacement then inevitably represents merely a lower limit.

Fig. 2b depicts the individual contributions to the effective penetration depth according to our heuristic model. Hereby, the thermal diffusion length is calculated with $\delta_{\mathrm{diff}} = \sqrt{2D_{\mathrm{th}}\tau_{\mathrm{p}}}$ with a thermal diffusivity of 3.5 $\mathrm{nm}^2/\mathrm{ps}$ [37]. This corresponds to the diffusion during τ_{p}, more precisely between $-\tau_{\mathrm{p}}/2$ and $\tau_{\mathrm{p}}/2$, where roughly 70 % of the total laser fluence is absorbed. From this we obtain a maximum diffusion length of about 12 nm at the 20 ps pulse duration. The resulting mechanical displacement, also at $\tau_{\mathrm{p}}/2$ is then 25 nm, so that the effective penetration depth is significantly reduced to 2.6(1.3) nm, which explains the strong discrepancy of δ_{eff} and δ_{opt} of 15.6(1) nm. For short pulse durations ($\tau_{\mathrm{p}} < \tau_{\mathrm{mech}}$) δ_{disp} roughly corresponds to the propagation of an acoustic wave in the liquid metal (Fig. 2b, dotted black line). With increasing pulse duration the material expansion proceeds slightly slower, and a sublinear dependence of the mechanical surface expansion at $\tau_{\mathrm{p}}/2$ on the pulse duration ($\delta_{\mathrm{disp}}(\tau_{\mathrm{p}}) < c_{\mathrm{s}}\tau_{\mathrm{p}}$, for $\tau_{\mathrm{p}} > \tau_{\mathrm{mech}}$) is found. This is in good agreement with the decrease of the maximum induced pressure buildup for pulse durations exceeding the mechanical relaxation time [25]. Nevertheless, due to the high electron localization of the CrMnFeCoNi alloy, yielding a low thermal conductivity and high electron phonon coupling, the situation of an attenuated stress confinement is still fulfilled, which leads to a sufficient buildup of thermoelastic pressures [17]. This decrease is also related to the sublinear increase of the surface expansion with pulse duration, where we obtain for 5, 10 and 20 ps values for δ_{disp} of 12, 20 and 25 nm, respectively (see Fig. 2b). A comparison of the calculated mechanical expansion at 2.5 Φ_{thr} with aluminum [29], which is already approximately 10 nm for a pulse duration of 0.7 ps (at $t = \tau_{\mathrm{p}}/2$), and a typical surface propagation velocity after pulse impact of 1 km/s [30], shows that our approximation is in the same order of magnitude but slightly underestimates the measurement. This observation is consistent with the preceding discussion on optical penetration depth, from which we expect a minimum value for δ_{disp}. We further may conclude, that above a certain pulse duration the increase of the thermal diffusion length exceeds that of the mechanical expansion, so that the effective penetration depth will start to raise once a minimum value is reached. Thus, interpretation of the increase in ablation efficiency for longer nanosecond pulses (starting from roughly 100 ns) [59] may also be tackled in conjunction with the heuristic model.

The ablation mechanism for our investigated pulse durations can also be discussed using scanning electron microscopy (SEM) images of the ablation craters. Fig. 2c shows the SEM images of the CrMnFeCoNi alloy at 0.5 ps (left) and 20 ps (right) pulse durations for a peak fluence of 0.9(1) $\mathrm{J/cm}^2$, which is close to the *ESAV* maximum. The corresponding crater cross sections are presented left and right, respectively, and the magnification of the marked region (yellow dashed line) is shown in Fig. 2d. For the 0.5 ps crater, nano-groves are revealed in the SEM image, which are mainly located near the ablation crater rim and occasionally inside the ablation crater. This occurrence is explained by the interaction of the laser irradiation with existing nano-scratches on the pristine surface, which are a leftover from the sample preparation by polishing (see Materials and Methods). This is causing a local field enhancement [39,60], and thus an increased ablation effect. In addition, the surface is strongly characterized by small ridged structures, the onset of melting jets with nano droplets, which indicate photomechanical spallation of a liquefied metal layer [61]. The corresponding crater cross-section is mainly parabolic with a small change in the slope at a depth of approx. 10 nm, which is referred to the formation of a spallation layer at the crater edge [62,63]. In contrast, the crater cross-section is more rectangular when processed with 20 ps pulses (see Fig. 2c and 2d, right). We

explain the transition between the two cross sections as follows. Since for our experiments the lateral axis fluence gradient is lower in comparison to the energy density decrease within the optical/effective penetration depth, namely by a factor of about 1000 ($w_0/\delta_{opt} \approx 1000$), the lateral heat fluxes may be neglect. Therefore we expect a nearly independent lateral fluence dependence of the ablation process, similar to a 1D approximation. From the evaluation of the effective penetration depths, we had found that processed with one pulse duration, the ablation depth scales logarithmic with the peak fluence. Therefore we conclude that the strength of the surface displacement also depends logarithmically on the lateral fluence distribution. Thus, for the 20 ps crater profile, the quadratic ablation cross section is explained by a paraboloid surface displacement ($\delta_{disp}(r) \propto \ln(\exp(-2r^2/w_0^2))$), which counteracts the primary parabolic crater cross section. In contrast to the 0.5 ps pulse duration, the crater surface for the 20 ps pulse reveals a smooth surface of already re-solidified material. This is due to the low thermal conductivity of the CrMnFeCoNi alloy, giving the molten metal enough time to form a smooth surface driven by the surface tension. In materials with high thermal conductivity, such as copper, or in a cooling medium, as is the case with laser ablation in liquids, strong melt jets are found under similar conditions [17,61,64]. The influence of the pulse duration-dependent heat diffusion and the resulting higher contribution of thermal processes, here in the form of liquefaction, can also be clearly seen at the crater edge. Here, in contrast to the 0.5 ps, less or only blurred nano-groves are observed. As a matter of fact, the laser peak intensity is still sufficient to produce a local field enhancement and consequently nano-groves (e.g. at the bottom right of the 20 ps ablation crater). At the crater edge, where the local applied fluence is far below the ablation threshold, thermal effects cannot completely wash out the nano-groves, as it is the case for the crater center.

5. Summary and conclusion

Using the CrMnFeCoNi alloy as substrate, we demonstrate the influence of the pulse duration on energetics and morphology of ultrashort pulse laser ablation in the limit of strong electron localization and subsequent weakest thermal conductivity and strongest electron–phonon coupling. The experimentally observed decreasing ablation efficiency is explained with our heuristic model by a decreasing effective penetration depth, which was not understood in the state of the art, because an increase of the effective penetration depth was expected for longer pulse durations. By choosing a model alloy with minimized heat diffusion, we were able to relate the decrease of the effective penetration depth to the onset of early mechanical surface expansion during the pulse irradiation, especially for pulses violating the stress confinement condition when exceeding the mechanical relaxation time of 4.5ps. Finally, by analyzing the effective penetration depth and its contributions, we showed that the strong electron localization in high-entropy alloys yields ideal ultrafast laser-induced stress confinement, which predicts the highest ablation efficiency for pulse durations below the mechanical relaxation time.

CRediT authorship contribution statement

David Redka: Conceptualization, Methodology, Investigation, Visualization, Writing – original draft. **Jan Winter:** Methodology, Validation, Writing – review & editing. **Christian Gadelmeier:** Investigation. **Alexander Djuranovic:** Investigation. **Uwe Glatzel:** Writing – review & editing. **Ján Minár:** Conceptualization, Supervision, Writing – original draft. **Heinz Paul Huber:** Conceptualization, Supervision, Writing – original draft.

Declaration of Competing Interest

The authors declare that they have no known competing financial interests or personal relationships that could have appeared to influence the work reported in this paper.

Acknowledgements

The authors greatly acknowledge the financial support of this work, which was provided by the Deutsche Forschungsgemeinschaft (DFG) through grants HU 1893/5-1 (project 423531130), HU 1893/6-1 (project 428315411), HU1893/7-1 (project 428973857) and GL 181/56-1. J.W. gratefully acknowledges the funding of the Erlangen Graduate School in Advanced Optical Technologies (SAOT) by the Bavarian State Ministry for Science and Art. J.M. would like to thank the CEDAMNF Project financed by the Ministry of Education, Youth and Sports of Czech Republic, Project No. CZ.02.1.01/0.0/0.0/15_003/0000358.

***Data** availability*

The data that underlie the figures in this work and supplementary materials are available from the corresponding authors upon request.

Appendix A. Supplementary material

Supplementary data to this article can be found online at https://doi.org/10.1016/j.apsusc.2022.153427.

References

[1] L.V. Zhigilei, Z. Lin, D.S. Ivanov, Atomistic modeling of short pulse laser ablation of metals: Connections between melting, spallation, and phase explosion, J. Phys. Chem. C 113 (2009) 11892–11906, https://doi.org/10.1021/jp902294m.
[2] J. Winter, S. Rapp, M. Schmidt, H.P. Huber, Ultrafast laser processing of copper: A comparative study of experimental and simulated transient optical properties, Appl. Surf. Sci. 417 (2017) 2–15, https://doi.org/10.1016/j.apsusc.2017.02.070.
[3] M.E. Povarnitsyn, V.B. Fokin, P.R. Levashov, Microscopic and macroscopic modeling of femtosecond laser ablation of metals, Appl. Surf. Sci. 357 (2015) 1150–1156, https://doi.org/10.1016/j.apsusc.2015.09.131.
[4] M.E. Povarnitsyn, P.R. Levashov, Simulation of single-, double- and multi-pulse laser ablation of metals, J. Phys. Conf. Ser. 1147 (2019), 012063, https://doi.org/10.1088/1742-6596/1147/1/012063.
[5] G. Raciukaitis, M. Brikas, M. Gedvilas, Efficiency aspects in processing of metals with high-repetition-rate ultra-short-pulse lasers. ICALEO 2008–27th Int, Congr. Appl. Lasers Electro-Optics, Congr. Proc., Laser Institute of Am. (2008) 176–184, https://doi.org/10.2351/1.5061377.
[6] B. Neuenschwander, B. Jaeggi, M. Schmid, V. Rouffiange, P.-E. Martin, Optimization of the volume ablation rate for metals at different laser pulse-durations from ps to fs, Laser Appl. Microelectron Optoelectron Manuf. XVII 8243 (2012), 824307, https://doi.org/10.1117/12.908583.
[7] B. Neuenschwander, T. Kramer, B. Lauer, B. Jaeggi, Burst mode with ps- and fs-pulses: Influence on the removal rate, surface quality, and heat accumulation, Laser Appl. Microelectron Optoelectron Manuf. XX 9350 (2015) 93500U, https://doi.org/10.1117/12.2076455.
[8] J. Lopez, R. Torres, Y. Zaouter, P. Georges, M. Hanna, E. Mottay, et al., Study on the influence of repetition rate and pulse duration on ablation efficiency using a new generation of high power ytterbium doped fiber ultrafast laser, Front Ultrafast Opt. Biomed. Sci. Ind. Appl. XIII 8611 (2013), 861118, https://doi.org/10.1117/12.2002080.
[9] Q. Li, L. Yang, C. Hou, O. Adeyemi, C. Chen, Y. Wang, Surface ablation properties and morphology evolution of K24 nickel based superalloy with femtosecond laser percussion drilling, Opt. Lasers Eng. 114 (2019) 22–30, https://doi.org/10.1016/j.optlaseng.2018.10.010.
[10] X. Sedao, M. Lenci, A. Rudenko, N. Faure, A. Pascale-Hamri, J.P. Colombier, C. Mauclair, Influence of pulse repetition rate on morphology and material removal rate of ultrafast laser ablated metallic surfaces, Opt. Lasers Eng. 116 (2019) 68–74.
[11] C. Momma, B.N. Chichkov, S. Nolte, F. von Alvensleben, A. Tünnermann, H. Welling, B. Wellegehausen, Short-pulse laser ablation of solid targets, Opt. Commun. 129 (1-2) (1996) 134–142.
[12] W. Schulz, U. Eppelt, R. Poprawe, Review on laser drilling I. Fundamentals, modeling, and simulation, J. Laser Appl. 25 (1) (2013) 012006.
[13] B. Neuenschwander, B. Jaeggi, M. Schmid, From fs to sub-ns: Dependence of the material removal rate on the pulse duration for metals, Phys. Procedia. 41 (2013) 794–801, https://doi.org/10.1016/j.phpro.2013.03.150.
[14] B.N. Chichkov, C. Momma, S. Nolte, F. von Alvensleben, A. Tünnermann, Femtosecond, picosecond and nanosecond laser ablation of solids, Appl. Phys. A Mater. Sci. Process 63 (1996) 109–115, https://doi.org/10.1007/s003390050359.
[15] R. Le Harzic, N. Huot, E. Audouard, C. Jonin, P. Laporte, S. Valette, A. Fraczkiewicz, R. Fortunier, Comparison of heat-affected zones due to

nanosecond and femtosecond laser pulses using transmission electronic microscopy, Appl. Phys. Lett. 80 (21) (2002) 3886–3888.
[16] M. Malinauskas, A. Žukauskas, S. Hasegawa, Y. Hayasaki, V. Mizeikis, R. Buividas, S. Juodkazis, Ultrafast laser processing of materials: from science to industry, Light Sci. Appl. 5 (8) (2016) e16133.
[17] J. Winter, M. Spellauge, J. Hermann, C. Eulenkamp, H.P. Huber, M. Schmidt, Ultrashort single-pulse laser ablation of stainless steel, aluminium, copper and its dependence on the pulse duration, Opt. Express 29 (2021) 14561, https://doi.org/10.1364/OE.421097.
[18] S. Nolte, C. Momma, H. Jacobs, A. Tünnermann, B.N. Chichkov, B. Wellegehausen, H. Welling, Ablation of metals by ultrashort laser pulses, J. Opt. Soc. Am. B 14 (10) (1997) 2716.
[19] C.K. Sun, F. Vallée, L.H. Acioli, E.P. Ippen, J.G. Fujimoto, Femtosecond-tunable measurement of electron thermalization in gold, Phys. Rev. B 50 (1994) 15337–15348, https://doi.org/10.1103/PhysRevB.50.15337.
[20] H.-T. Chang, A. Guggenmos, S.K. Cushing, Y. Cui, N.U. Din, S.R. Acharya, I. J. Porter, U. Kleineberg, V. Turkowski, T.S. Rahman, D.M. Neumark, S.R. Leone, Electron thermalization and relaxation in laser-heated nickel by few-femtosecond core-level transient absorption spectroscopy, Phys. Rev. B 103 (6) (2021), 064305, https://doi.org/10.1103/PhysRevB.103.064305.
[21] N. Del Fatti, R. Bouffanais, F. Vallée, C. Flytzanis, Nonequilibrium electron interactions in metal films, Phys. Rev. Lett. 81 (1998) 922–925, https://doi.org/10.1103/PhysRevLett.81.922.
[22] B. Rethfeld, D.S. Ivanov, M.E. Garcia, S.I. Anisimov, Modelling ultrafast laser ablation, J. Phys. D Appl. Phys. 50 (19) (2017) 193001.
[23] S.I. Anisimov, B.L. Kapeliovich, T. Perelman, et al., Electron emission from metal surfaces exposed to ultrashort laser pulses, Zh. Eksp. Teor. Fiz. 66 (1974) 375–377.
[24] D.S. Ivanov, B. Rethfeld, The effect of pulse duration on the interplay of electron heat conduction and electron-phonon interaction: Photo-mechanical versus photo-thermal damage of metal targets, Appl. Surf. Sci. 255 (2009) 9724–9728, https://doi.org/10.1016/j.apsusc.2009.04.131.
[25] G. Paltauf, P.E. Dyer, Photomechanical processes and effects in ablation, Chem. Rev. 103 (2003) 487–518, https://doi.org/10.1021/cr010436c.
[26] E. Leveugle, D.S. Ivanov, L.V. Zhigilei, Photomechanical spallation of molecular and metal targets: Molecular dynamics study, Appl. Phys. A Mater. Sci. Process 79 (2004) 1643–1655, https://doi.org/10.1007/s00339-004-2682-2.
[27] C. Wu, L.V. Zhigilei, Microscopic mechanisms of laser spallation and ablation of metal targets from large-scale molecular dynamics simulations, Appl. Phys. A Mater. Sci. Process 114 (2014) 11–32, https://doi.org/10.1007/s00339-013-8086-4.
[28] M.E. Povarnitsyn, T.E. Itina, P.R. Levashov, K.V. Khishchenko, Simulation of ultrashort double-pulse laser ablation, Appl. Surf. Sci. 257 (2011) 5168–5171, https://doi.org/10.1016/j.apsusc.2010.11.158.
[29] J. Winter, S. Rapp, M. Spellauge, C. Eulenkamp, M. Schmidt, H.P. Huber, Ultrafast pump-probe ellipsometry and microscopy reveal the surface dynamics of femtosecond laser ablation of aluminium and stainless steel, Appl. Surf. Sci. 511 (2020), 145514, https://doi.org/10.1016/j.apsusc.2020.145514.
[30] Fourment C, Deneuville F, Chimier B, Descamps D, Dorchies F, Hulin S, et al. An interferometric diagnostic for the experimental study of dynamics of solids exposed to intense and ultrashort radiation. Damage to VUV, EUV, X-Ray Opt IV; EUV X-Ray Opt Synerg between Lab Sp III 2013;8777:87770M. https://doi.org/10.1117/12.2018982.
[31] A. Miotello, R. Kelly, Laser-induced phase explosion: New physical problems when a condensed phase approaches the thermodynamic critical temperature, Appl. Phys. A Mater. Sci. Process 69 (1999) 67–73, https://doi.org/10.1007/s003390051357.
[32] J. Furmanski, A.M. Rubenchik, M.D. Shirk, B.C. Stuart, Deterministic processing of alumina with ultrashort laser pulses, J. Appl. Phys. 102 (7) (2007) 073112.
[33] N.A. Smirnov, S.I. Kudryashov, P.A. Danilov, A.A. Rudenko, B. Gakovic, D. Milovanović, A.A. Ionin, A.A. Nastulyavichus, S.F. Umanskaya, Microprocessing of a steel surface by single pulses of variable width, Laser Phys. Lett. 16 (5) (2019) 056002, https://doi.org/10.1088/1612-202X/ab0c85.
[34] B. Cantor, I.T.H. Chang, P. Knight, A.J.B. Vincent, Microstructural development in equiatomic multicomponent alloys, Mater. Sci. Eng. A 375–377 (2004) 213–218, https://doi.org/10.1016/j.msea.2003.10.257.
[35] S. Mu, G.D. Samolyuk, S. Wimmer, M.C. Troparevsky, S.N. Khan, S. Mankovsky, H. Ebert, G.M. Stocks, Uncovering electron scattering mechanisms in NiFeCoCrMn derived concentrated solid solution and high entropy alloys, Npj. Comput. Mater 5 (1) (2019), https://doi.org/10.1038/s41524-018-0138-z.
[36] K. Jin, B.C. Sales, G.M. Stocks, G.D. Samolyuk, M. Daene, W.J. Weber, Y. Zhang, H. Bei, Tailoring the physical properties of Ni-based single-phase equiatomic alloys by modifying the chemical complexity, Sci. Rep. 6 (1) (2016), https://doi.org/10.1038/srep20159.
[37] K. Jin, S. Mu, K. An, W.D. Porter, G.D. Samolyuk, G.M. Stocks, H. Bei, Thermophysical properties of Ni-containing single-phase concentrated solid solution alloys, Mater. Des. 117 (2017) 185–192.
[38] F. Körmann, Y. Ikeda, B. Grabowski, M.H.F. Sluiter, Phonon broadening in high entropy alloys, Npj. Comput. Mater. 3 (2017) 36, https://doi.org/10.1038/s41524-017-0037-8.
[39] D. Redka, C. Gadelmeier, J. Winter, M. Spellauge, C. Eulenkamp, P. Calta, U. Glatzel, J. Minár, H.P. Huber, Sub-picosecond single-pulse laser ablation of the CrMnFeCoNi high entropy alloy and comparison to stainless steel AISI 304, Appl. Surf. Sci. 544 (2021) 148839, https://doi.org/10.1016/j.apsusc.2020.148839.
[40] C. Gadelmeier, S. Haas, T. Lienig, A. Manzoni, M. Feuerbacher, U. Glatzel, Temperature dependent solid solution strengthening in the high entropy alloy CrMnFeCoNi in single crystalline state, Metals (Basel) 10 (2020) 1–13, https://doi.org/10.3390/met10111412.
[41] O.E. Martinez, J.P. Gordon, R.L. Fork, Negative group-velocity dispersion using refraction, J. Opt. Soc. Am. A 1 (1984) 1003, https://doi.org/10.1364/josaa.1.001003.
[42] V. Chauhan, P. Bowlan, J. Cohen, R. Trebino, Single-diffraction-grating and grism pulse compressors, J. Opt. Soc. Am. B 27 (2010) 619, https://doi.org/10.1364/josab.27.000619.
[43] J.M. Liu, Simple technique for measurements of pulsed Gaussian-beam spot sizes, Opt. Lett. 7 (1982) 196, https://doi.org/10.1364/ol.7.000196.
[44] M. Domke, L. Nobile, S. Rapp, S. Eiselen, J. Sotrop, H.P. Huber, M. Schmidt, Understanding thin film laser ablation: The role of the effective penetration depth and the film thickness, Phys. Procedia. 56 (2014) 1007–1014.
[45] B.C. Stuart, M.D. Feit, S. Herman, A.M. Rubenchik, B.W. Shore, M.D. Perry, Optical ablation by high-power short-pulse lasers, J. Opt. Soc. Am. B 13 (1996) 459, https://doi.org/10.1364/josab.13.000459.
[46] H. Mustafa, R. Pohl, T.C. Bor, B. Pathiraj, D.T.A. Matthews, G.R.B.E. Römer, Picosecond-pulsed laser ablation of zinc: crater morphology and comparison of methods to determine ablation threshold, Opt. Express 26 (2018) 18664, https://doi.org/10.1364/oe.26.018664.
[47] G. Račiukaitis, M. Brikas, P. Gečys, B. Voisiat, M. Gedvilas, Use of high repetition rate and high power lasers in microfabrication: How to keep the efficiency high? J. Laser. Micro. Nanoeng. 4 (2009) 186–191, https://doi.org/10.2961/jlmn.2009.03.0008.
[48] L.V. Zhigilei, B.J. Garrison, Mechanisms of laser ablation from molecular dynamics simulations: Dependence on the initial temperature and pulse duration, Appl. Phys. A Mater. Sci. Process 69 (1999) S75–S80, https://doi.org/10.1007/s003399900347.
[49] S. Blairs, Temperature dependence of sound velocity in liquid metals, Phys. Chem. Liq. 44 (2006) 597–606, https://doi.org/10.1080/00319100600932200.
[50] M. Bonn, D.N. Denzler, S. Funk, M. Wolf, S.S. Wellershoff, J. Hohlfeld, Ultrafast electron dynamics at metal surfaces: Competition between electron-phonon coupling and hot-electron transport, Phys. Rev. B - Condens Matter Mater. Phys. 61 (2000) 1101–1105, https://doi.org/10.1103/PhysRevB.61.1101.
[51] E. Bévillon, J.P. Colombier, V. Recoules, R. Stoian, Free-electron properties of metals under ultrafast laser-induced electron-phonon nonequilibrium: A first-principles study, Phys. Rev. B - Condens Matter Mater. Phys. 89 (2014) 1–13, https://doi.org/10.1103/PhysRevB.89.115117.
[52] Z. Lin, L.V. Zhigilei, V. Celli, Electron-phonon coupling and electron heat capacity of metals under conditions of strong electron-phonon nonequilibrium, Phys. Rev. B – Condens. Matter Mater. Phys. 77 (2008) 1–17, https://doi.org/10.1103/PhysRevB.77.075133.
[53] E. Bévillon, J.P. Colombier, B. Dutta, R. Stoian, Ab initio nonequilibrium thermodynamic and transport properties of ultrafast laser irradiated 316l stainless steel, J. Phys. Chem. C 119 (2015) 11438–11446, https://doi.org/10.1021/acs.jpcc.5b02085.
[54] P. Lickschat, D. Metzner, S. Weißmantel, Fundamental investigations of ultrashort pulsed laser ablation on stainless steel and cemented tungsten carbide, Int. J. Adv. Manuf. Technol. 109 (2020) 1167–1175, https://doi.org/10.1007/s00170-020-05502-8.
[55] D. Metzner, M. Olbrich, P. Lickschat, A. Horn, S. Weißmantel, Experimental and Theoretical Determination of the Effective Penetration Depth of Ultrafast Laser Radiation in Stainless Steel, Lasers Manuf. Mater. Process 7 (2020) 478–495, https://doi.org/10.1007/s40516-020-00129-9.
[56] E. Bévillon, R. Stoian, J.P. Colombier, Nonequilibrium optical properties of transition metals upon ultrafast electron heating, J. Phys. Condens Matter 30 (38) (2018) 385401, https://doi.org/10.1088/1361-648X/aad8e5.
[57] S. Wang, T. Zhang, H. Hou, Y. Zhao, The Magnetic, Electronic, and Thermodynamic Properties of High Entropy Alloy CrMnFeCoNi: A First-Principles Study, Phys. Status Solidi Basic Res. 255 (2018) 1–6, https://doi.org/10.1002/pssb.201800306.
[58] J. Winter, J. Sotrop, S. Borek, H.P. Huber, J. Minár, Temperature-dependent determination of electron heat capacity and electron-phonon coupling factor for Fe0.72Cr0.18Ni0.1, Phys. Rev. B 93 (2016) 1–8, https://doi.org/10.1103/PhysRevB.93.165119.
[59] D.J. Förster, B. Jäggi, A. Michalowski, B. Neuenschwander, Review on Experimental and Theoretical Investigations of Ultra-Short Pulsed Laser Ablation of Metals with Burst Pulses, Materials (Basel) 14 (2021) 3331, https://doi.org/10.3390/ma14123331.
[60] A. Rudenko, C. Mauclair, F. Garrelie, R. Stoian, J.P. Colombier, Light absorption by surface nanoholes and nanobumps, Appl. Surf. Sci. 470 (2019) 228–233, https://doi.org/10.1016/j.apsusc.2018.11.111.
[61] S.I. Ashitkov, N.A. Inogamov, V.V. Zhakhovskii, Y.N. Emirov, M.B. Agranat, I. I. Oleinik, S.I. Anisimov, V.E. Fortov, Formation of nanocavities in the surface layer of an aluminum target irradiated by a femtosecond laser pulse, JETP Lett. 95 (4) (2012) 176–181.
[62] I. Mirza, N.M. Bulgakova, J. Tomáštík, V. Michálek, O. Haderka, L. Fekete, et al., Ultrashort pulse laser ablation of dielectrics: Thresholds, mechanisms, role of breakdown, Sci. Rep. 6 (2016) 39133, https://doi.org/10.1038/srep39133.
[63] C. Körner, R. Mayerhofer, M. Hartmann, H.W. Bergmann, Physical and material aspects in using visible laser pulses of nanosecond duration for ablation, Appl. Phys. A Mater. Sci. Process 63 (1996) 123–131, https://doi.org/10.1007/bf01567639.
[64] C.-Y. Shih, I. Gnilitskyi, M.V. Shugaev, E. Skoulas, E. Stratakis, L.V. Zhigilei, Effect of a liquid environment on single-pulse generation of laser induced periodic surface structures and nanoparticles, Nanoscale 12 (14) (2020) 7674–7687.